Comparison of Kalman-filter-based approaches for block matching in arterial wall motion analysis from B-mode ultrasound

2011 Meas. Sci. Technol. 22 114008

(http://iopscience.iop.org/0957-0233/22/11/114008)

Meas. Sci. Technol. **22** (2011) 114008 (9pp) doi:10.1088/0957-0233/22/11/114008

Comparison of Kalman-filter-based approaches for block matching in arterial wall motion analysis from B-mode ultrasound

A Gastounioti[1], S Golemati[2], J Stoitsis[1] and K S Nikita[1]

[1] Biomedical Simulations and Imaging Laboratory, National Technical University of Athens, Athens, Greece
[2] First Intensive Care Unit, Medical School, National and Kapodistrian University of Athens, Athens, Greece

E-mail: stoitsis@biosim.ntua.gr, knikita@ece.ntua.gr, sgolemati@med.uoa.gr and gaimilia@biosim.ntua.gr

Received 15 December 2010, in final form 7 July 2011
Published 14 October 2011
Online at stacks.iop.org/MST/22/114008

Abstract
Block matching (BM) has been previously used to estimate motion of the carotid artery from B-mode ultrasound image sequences. In this paper, Kalman filtering (KF) was incorporated in this conventional method in two distinct scenarios: (a) as an adaptive strategy, by renewing the reference block and (b) by renewing the displacements estimated by BM or adaptive BM. All methods resulting from combinations of BM and KF with the two scenarios were evaluated on synthetic image sequences by computing the warping index, defined as the mean squared error between the real and estimated displacements. Adaptive BM, followed by an update through the second scenario at the end of tracking, ABM_KF-K2, minimized the warping index and yielded average displacement error reductions of 24% with respect to BM. The same method decreased estimation bias and jitter over varying center frequencies by 30% and 64%, respectively, with respect to BM. These results demonstrated the increased accuracy and robustness of ABM_KF-K2 in motion tracking of the arterial wall from B-mode ultrasound images, which is crucial in the study of mechanical properties of normal and diseased arterial segments.

Keywords: Kalman filter, block matching, motion analysis, ultrasound, arterial wall

1. Introduction

B-mode ultrasound imaging is a relatively inexpensive, fast, noninvasive and radiation-free imaging technique, which is widely used in the diagnosis of arterial disease. This imaging technique can be used to study arterial wall motion during the cardiac cycle by recording image sequences and subsequently applying a motion estimation algorithm.

Block matching (BM) is a straightforward motion estimation algorithm, which relies on the use of a reference block of pixels in the first image of the sequence and the identification, in each subsequent image, of a block that shows the highest similarity to the reference block. The method has been previously used to estimate carotid artery wall motion from B-mode ultrasound [1–4]. Specifically, BM has been applied to real ultrasound image sequences of the carotid artery to estimate the vessel diameter in systole and diastole and the arterial wall distensibility in the radial and longitudinal directions [1]. Cinthio *et al* used the same method to study the average motion amplitude and the shear strain within the wall [2]. BM was also selected by Bang *et al* [3] to study motion dynamics of carotid atheromatous plaque. In addition to the above, BM was used to show that scanner settings, such as the dynamic range and the persistence, do not significantly alter radial and longitudinal carotid artery motion estimation [4].

The conventional BM algorithm focuses on estimating the motion field between specific image pairs of a sequence, disregarding estimates obtained from previous image pairs. Several attempts have been made to effectively incorporate the temporal dimension into the motion estimation process. One of these attempts included adaptive block matching (ABM), an extension of the conventional BM, which updates the reference block considering one or more of the previous frames. Four update strategies have been proposed, namely single-frame, multiframe, finite impulse response filtering and Kalman filtering (KF), and it was shown that the use of KF was the most robust strategy which minimized the mean tracking error [5]. The methods were also used to extract motor activity signals of selected anatomical sites from video recordings of neonatal seizures and the best performance was again achieved when KF was used [6]. A simple one-dimensional (1D) KF was applied, both as a post-processing and an embedded method, to enhance the performance of motion estimation techniques in low or very low bit rate applications such as videoconference and videophone where conventional algorithms, such as BM, were not effective enough [7]. In [8], the incorporation of KF in motion tracking showed that taking into consideration the temporal coherence of motion throughout an image sequence resulted in considerable improvement in the quality of motion estimation for large amplitudes of movement. The update of motion estimates within the KF formalism also behaved very well at discontinuities of the motion field [9]. Moreover, KF has been implemented to recursively predict and update contour deformations in real time, aiming at automatic tracking of myocardial borders in two-dimensional [10, 11] or three-dimensional [12] echocardiography.

The increased accuracy in motion tracking provided by KF in the above applications, along with the fact that the accuracy in arterial wall motion estimation is an important clinical challenge not adequately addressed in the literature, motivated the investigation of the performance of KF-based motion estimators in this clinical area, where only conventional algorithms have been used. The underlying ideas were first introduced in a preliminary study of our group [13], where KF was used (a) as an ABM strategy (ABM_KF), and to renew the estimate of BM (b) during and (c) at the end of tracking. The application of those three methods to B-mode ultrasound image sequences of the carotid artery was encouraging, suggesting that the potential of KF to enhance the accuracy of BM in motion estimation is worth further investigation.

Based on the above, this work systematically investigates the potential of KF-based methodologies to accurately detect carotid arterial wall motion from B-mode ultrasound. To this end, a thorough optimization of the methods proposed in [13] was performed on noise-free and noisy synthetic image sequences of the common carotid artery. Additionally, these methods were implemented in different scenarios, with KF being used to renew the estimate of both BM and ABM_KF during or/and at the end of tracking. Thus, a total of seven KF-based motion estimators were produced which were compared with the conventional BM. All methods were evaluated on synthetic image sequences of the common carotid artery with varying noise levels and center frequencies. Finally, the performance of the most accurate algorithm according to the synthetic data experiments was further assessed through detailed experiments on real ultrasound image sequences of the carotid artery of nine normal subjects.

2. Basic principles of KF

KF is an efficient recursive filter that estimates the current state of a linear dynamic system from a series of noisy measurements [14]. It assumes that the true state of the system at time k is related to the state at time $(k-1)$ according to the process model:

$$\boldsymbol{x}_k = \boldsymbol{A}x_{k-1} + \boldsymbol{B}u_k + \boldsymbol{w}_k, \tag{1}$$

where $\boldsymbol{x}_k$ is the state at time k, $\boldsymbol{A}$ is the state transition matrix applied to the previous state $\boldsymbol{x}_{k-1}$, $\boldsymbol{B}$ is the control-input matrix applied to the control vector $\boldsymbol{u}_k$ and $\boldsymbol{w}_k$ is the process noise with a zero mean normal distribution described by the covariance matrix $\boldsymbol{Q}$. At time k, an observation, or measurement, $\boldsymbol{z}_k$ of the true state $\boldsymbol{x}_k$ is made according to the measurement model:

$$\boldsymbol{z}_k = \boldsymbol{H}\boldsymbol{x}_k + v_k, \tag{2}$$

where $\boldsymbol{H}$ relates the measurement of the true state to the true state and $\boldsymbol{v}_k$ is the observation noise, the distribution of which is described by the covariance matrix $\boldsymbol{C}$. To use KF, one should model the process according to the above equations.

Because KF is a recursive estimator, only the estimated state from the previous time step ($\hat{\boldsymbol{x}}_{k-1}$) and the current measurement ($\boldsymbol{z}_k$) are needed to compute the estimate for the current state ($\hat{\boldsymbol{x}}_k$). KF acts in two distinct phases: prediction and update. The prediction phase produces an *a priori* estimate of the state ($\hat{\boldsymbol{x}}_k^-$) and the filter's error, the distribution of which is represented by the covariance matrix ($\boldsymbol{P}_k^-$):

$$\hat{\boldsymbol{x}}_k^- = \boldsymbol{A}\hat{\boldsymbol{x}}_{k-1} + \boldsymbol{B}\boldsymbol{u}_{k-1} \tag{3}$$

$$\boldsymbol{P}_k^- = \boldsymbol{A}\boldsymbol{P}_{k-1}\boldsymbol{A}^{\mathrm{T}} + \boldsymbol{Q}. \tag{4}$$

In the update phase, the *a priori* estimate is considered as a linear combination of the *a priori* state estimate and the difference (multiplied with an appropriate factor) between the observation and the prediction of the observation:

$$\hat{\boldsymbol{x}}_k = \hat{\boldsymbol{x}}_k^- + \boldsymbol{K}(\boldsymbol{z}_k - \boldsymbol{H}\hat{\boldsymbol{x}}_k^-). \tag{5}$$

This factor is represented by the Kalman gain $\boldsymbol{K}$:

$$\boldsymbol{K} = \boldsymbol{P}_k^-\boldsymbol{H}^{\mathrm{T}}(\boldsymbol{H}\boldsymbol{P}_k^-\boldsymbol{H}^{\mathrm{T}} + \boldsymbol{C})^{-1}. \tag{6}$$

The improved estimate is termed the *a posteriori* estimate of the current state ($\hat{\boldsymbol{x}}_k$) and the filter's error is updated according to the following equation:

$$\boldsymbol{P}_k = (\boldsymbol{I} - \boldsymbol{K}\boldsymbol{H})\boldsymbol{P}_k^-. \tag{7}$$

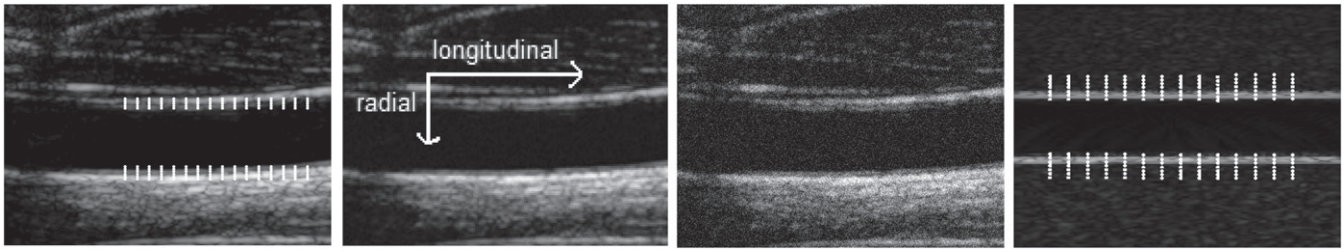

(*a*) (*b*) (*c*) (*d*)

Figure 1. Examples of images of the common carotid artery wall in synthetic sequences: (*a*) S_0, (*b*) S_{25}, (*c*) S_{15} and (*d*) S_F. The white marks represent the selected block centers.

3. Methods

3.1. Synthetic image data

All presented methods were optimized in terms of their parameters and they were evaluated by applying them to four synthetic 87-image sequences of the common carotid artery, corresponding to three cardiac cycles. The first synthetic sequence (S_0) was created by distorting a real ultrasonic B-mode image (see section 3.2) according to a mathematical motion model [15]. Two additional sequences, S_{25} and S_{15}, were created by corrupting the first sequence with Gaussian noise with signal-to-noise ratios equal to 25 and 15 dB, respectively. The fourth synthetic sequence (S_F) was constructed from a sequence of scattering strength maps according to the procedures described in [15], using the field II software package [16] and the same mathematical motion model. Figure 1 presents the first images of the four synthetic sequences.

The evaluation process of the methods was also dependent on their performance over different imaging settings. Taking into consideration that for S_0, S_{25} and S_{15} these settings are fixed at image acquisition, additional synthetic image sequences were produced with field II and varying center frequencies. Specifically, seven sequences were created, using values of 5, 5.5, 6, 6.5, 7, 7.5 and 8 MHz, which are frequently used in B-mode ultrasound imaging of the carotid artery. The center frequency was selected for this investigation because in the evaluation of a 1D motion estimator, it produced higher standard deviations of errors than other imaging parameters [17], suggesting that it strongly affects the accuracy in motion estimation.

Performance was assessed by means of the warping index (w) defined by (8)–(10), separately for the longitudinal (w_{long}), radial (w_{rad}) and total (w_{total}) displacements, respectively:

$$w_{\text{long}} = \sqrt{\frac{\sum_{j=1}^{m}\sum_{i=1}^{n}(\text{long}_{\text{real}}(j,i) - \text{long}_{\text{est}}(j,i))^2}{n \cdot m}} \quad (8)$$

$$w_{\text{rad}} = \sqrt{\frac{\sum_{j=1}^{m}\sum_{i=1}^{n}(\text{rad}_{\text{real}}(j,i) - \text{rad}_{\text{est}}(j,i))^2}{n \cdot m}} \quad (9)$$

$$w_{\text{total}} = \sqrt{w_{\text{long}}^2 + w_{\text{rad}}^2}, \quad (10)$$

where $\text{long}_{\text{real}}$ and rad_{real} are the real longitudinal and radial displacements, respectively, long_{est} and rad_{est} are the longitudinal and radial displacements, respectively, estimated by the algorithms, m is the number of selected blocks and n is the number of images of each sequence. Accordingly, w is the mean squared error between the real and estimated displacements and it represents an overall estimate of the error for all interrogated blocks and all images of the sequence.

The warping index was computed by choosing 176 block centers for sequences S_0, S_{25} and S_{15}, and 196 block centers for the sequence S_F. Figures 1(*a*) and (*d*) show examples of the selected block centers in the synthetic image sequences.

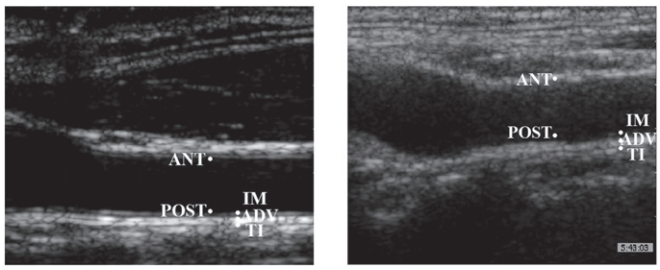

(*a*) (*b*)

Figure 2. The first frame of an ultrasound image sequence of (*a*) a young and (*b*) an elderly normal subject. The centers of the selected blocks are shown with white marks.

3.2. Real image data

To investigate the performance of the proposed methods in real data, nine real ultrasound image sequences of the carotid artery were used; five of young (ages: 25–32 years) and four of elderly (ages: 44–73 years) normal subjects. The sequences were recorded with an ATL (Advanced Technology Laboratory) Ultramark 4 Duplex scanner and a high-resolution 7.5 MHz linear scan head. Scanner settings were as follows: dynamic range 60 dB, 2D gray map, persistence low, frame rate high. The sequences were recorded at a rate of 25 frames s^{-1} for approximately 3 s (two to three cardiac cycles). Examples of the first frames of these sequences are shown in figure 2.

The real data experiments were conducted in accordance with the principles embodied in the Declaration of Helsinki, were approved by the local institutional review board and all individuals included in the study gave their informed consent to ultrasound imaging and to the scientific use of the data.

Table 1. ABM_KF, K1 and K2 optimal parameter values for the sequences S_0, S_{25}, S_{15} and S_F.

	ABM_KF			K1			K2		
	q	c	p_0	q	c	p_0	q	c	p_0
S_0	0.01	11	0.11	9.10	2.70	0.11	2.70	2.10	0.60
S_{25}	0.01	41	0.06	7.05	3.10	0.11	3.10	2.60	0.16
S_{15}	5.01	91	0.01	2.10	4.30	0.10	1.10	3.60	0.11
S_F	0.01	1	0.31	8.10	3.70	0.36	3.90	2.10	0.30

3.3. Block matching

BM assumes that a block of pixels remains constant over motion and that all its pixels have the same velocity. The algorithm consists in finding a block (best-matched block) in an image that shows the highest similarity to the reference block which is chosen by the user in the first image [18]. The search for the best-matched block is performed in a limited image region, called search window, around the best-matched block of the previous image.

The performance of the algorithm is affected by the similarity measure, the size and the location of the reference block, and the size of the search window. A large reference block improves the performance because it enhances the uniqueness of the block but, if it is too large, the computational cost increases. In terms of the location of the reference block, the heterogeneity of the interrogated area improves the performance. Finally the search window should be large enough so as to include the expected motion without entailing high computational cost.

In this work, BM methods were implemented in Matlab (The MathWorks, Natick, MA, USA), using (a) the correlation coefficient as the similarity measure, (b) 1.6×1 mm^2 reference blocks selected in the first frame and (c) 1.3×1.3 mm^2 search windows. The similarity measure and the size of the search window were suggested in [1] as the most appropriate for this application. The selection of the size of the reference blocks was based on experimentation with different sizes, varying between 0.7×0.7 [2] and 3.2×2.5 mm^2 [1], in an attempt to achieve a compromise between low warping indices and low computational cost.

3.4. ABM using KF

In ABM, the reference block is updated to take into consideration the changes in the appearance of the target [5]. KF can be used in ABM because it can estimate the reference block used for image k by modeling the process as

$$\boldsymbol{R}_k = \boldsymbol{R}_{k-1} + \boldsymbol{w}_k \tag{11}$$

$$\boldsymbol{M}_{k-1} = \boldsymbol{R}_{k-1} + \boldsymbol{v}_k, \tag{12}$$

where $\boldsymbol{R}$ is the reference block and $\boldsymbol{M}$ is the best-matched block. With reference to (1) and (2), $\boldsymbol{A} = \boldsymbol{H} = \boldsymbol{I}$ and $\boldsymbol{B} = 0$. Consequently, (3)–(7) are valid for $\boldsymbol{x} \equiv \boldsymbol{R}$ and $\boldsymbol{z}_k \equiv \boldsymbol{M}_{k-1}$.

The matrices $\boldsymbol{Q}$, $\boldsymbol{C}$ and $\boldsymbol{P}_0$ were considered proportional to the identity ($\boldsymbol{Q} = q\boldsymbol{I}$, $\boldsymbol{C} = c\boldsymbol{I}$, $\boldsymbol{P} = p_0\boldsymbol{I}$) [19] and the method was optimized in terms of the multiplication factors q, c and p_0. Experimentation with these parameters and computation of the corresponding warping indices showed that ABM_KF generally maximized its performance when $c > q$ and $p_0 \leqslant 0.31$, while greater noise levels required higher observation noise. This observation showed that the error was minimized when the measurement was considered less reliable than the *a priori* state estimate, which suggests that each image tended to use the previous reference block as a reference block, with a slight improvement derived from the difference between the best-matched block and the reference block of the previous image.

The optimal KF parameter values were different for each sequence (table 1). Therefore, ABM_KF was then applied to all sequences, using each set of optimal parameter values, and it was investigated which set produced the lowest mean warping index for total displacements. The results showed that the first set, i.e. the optimal parameter values for S_0, was the most suitable choice and it was used for both the evaluation of the method (section 4.1) and the real data experiments.

3.5. Updating motion estimation using KF

KF can be used to improve motion detection, by updating an algorithm's estimate for the position of the target throughout an image sequence. The above can be achieved by modeling the process as

$$\begin{bmatrix} r(k) \\ l(k) \\ \mathrm{d}r(k) \\ \mathrm{d}l(k) \end{bmatrix} = \begin{bmatrix} 1 & 0 & 1 & 0 \\ 0 & 1 & 0 & 1 \\ 0 & 0 & 1 & 0 \\ 0 & 0 & 0 & 1 \end{bmatrix} \begin{bmatrix} r(k-1) \\ l(k-1) \\ \mathrm{d}r(k-1) \\ \mathrm{d}l(k-1) \end{bmatrix} + w_k \tag{13}$$

where l and r are the coordinates of a pixel in the longitudinal and radial direction, respectively, and dl and dr are the corresponding displacements with respect to the previous image. The estimate of a motion-tracking algorithm, i.e. BM or ABM_KF, for the coordinates of the pixel at image k is considered as observation information:

$$\begin{bmatrix} zr(k) \\ zl(k) \end{bmatrix} = \begin{bmatrix} 1 & 0 & 0 & 0 \\ 0 & 1 & 0 & 0 \end{bmatrix} \begin{bmatrix} r(k) \\ l(k) \\ \mathrm{d}r(k) \\ \mathrm{d}l(k) \end{bmatrix} + v_k. \tag{14}$$

This idea can be implemented during (K1) or/and after (K2) the execution of an algorithm.

In this case, performance was still dependent on the matrices $\boldsymbol{Q}$, $\boldsymbol{C}$ and $\boldsymbol{P}_0$ which were defined in the same way as previously. Consequently, the methods were again optimized in terms of the multiplication factors q, c and p_0 (table 1). The warping indices for different parameter sets showed that K1 and K2 minimized their deviation from real motion when $c < q$ for S_0, S_{25} and S_F and $c > q$ for S_{15}. Additionally, as in ABM_KF, greater noise levels required higher observation

Table 2. Warping indices (in mm) for BM, ABM_KF and combinations of them with K1 and K2, for the sequences S_0, S_{25}, S_{15} and S_F. Boldface indicates minimum warping indices for total displacements for each sequence.

Algorithm	$\boldsymbol{w}_{\text{total}}$	$\boldsymbol{w}_{\text{rad}}$	$\boldsymbol{w}_{\text{long}}$	Algorithm	$\boldsymbol{w}_{\text{total}}$	$\boldsymbol{w}_{\text{rad}}$	$\boldsymbol{w}_{\text{long}}$
S_0				S_{25}			
BM	0.085	0.069	0.051	BM	0.314	0.071	0.306
BM-K1	**0.084**	0.052	0.065	BM-K1	0.361	0.054	0.357
BM-K2	**0.084**	0.069	0.048	BM-K2	0.312	0.071	0.304
BM-K1-K2	0.086	0.054	0.067	BM-K1-K2	0.361	0.056	0.357
ABM_KF	0.085	0.068	0.051	ABM_KF	0.266	0.070	0.257
ABM_KF-K1	0.118	0.049	0.108	ABM_KF-K1	0.361	0.051	0.367
ABM_KF-K2	**0.084**	0.069	0.048	ABM_KF-K2	**0.265**	0.070	0.256
ABM_KF-K1-K2	0.120	0.051	0.109	ABM_KF-K1-K2	0.361	0.054	0.357
S_{15}				S_F			
BM	1.176	0.296	1.139	BM	0.257	0.067	0.249
BM-K1	1.216	0.282	1.183	BM-K1	0.248	0.049	0.243
BM-K2	1.174	0.291	1.138	BM-K2	0.257	0.067	0.249
BM-K1-K2	1.217	0.280	1.184	BM-K1-K2	0.248	0.049	0.243
ABM_KF	0.985	0.344	0.923	ABM_KF	**0.095**	0.072	0.063
ABM_KF-K1	**1.054**	0.337	0.999	ABM_KF-K1	0.097	0.074	0.065
ABM_KF-K2	0.983	0.342	0.922	ABM_KF-K2	**0.095**	0.072	0.063
ABM_KF-K1-K2	**1.054**	0.337	0.999	ABM_KF-K1-K2	0.097	0.074	0.065

noise and lower values of p_0. According to these observations, the measurement was considered more reliable than the *a priori* estimate in noise-free sequences and in the presence of low noise levels. However, its reliability decreased with increasing noise levels and under very noisy conditions, i.e. for S_{15}, the methods required higher confidence to the process model.

Following the same process as in ABM_KF for the selection of parameter values to be held constant across different data sets, the optimal parameter values for S_0 were again selected for the evaluation process of both K1 and K2, as well as the real data experiments.

The combinations of BM and ABM_KF with K1 produced BM-K1 and ABM_KF-K1. The corresponding combinations with K2 produced BM-K2 and ABM_KF-K2. K2 was also combined with BM-K1 and ABM_KF-K1; specifically, it was applied at the end of the corresponding algorithms, resulting in BM-K1-K2 and ABM_KF-K1-K2, respectively. Accordingly, the previous combinations produced a total of seven methods that were compared with BM.

4. Results

4.1. Synthetic image sequences

Table 2 shows the warping indices for each synthetic sequence when motion was estimated by BM, ABM_KF and combinations of these methods with K1 and K2. As expected, the warping indices increased with increasing noise levels for all methods. In most cases, errors in the longitudinal direction were larger than in the radial one, which was more obvious in the cases of the noisy sequences S_{25} and S_{15}.

Generally the combinations of BM with K1 and K2 produced higher total motion-tracking errors than the combinations of ABM_KF with these methods. ABM_KF-K2 minimized the warping indices for total displacements in three out of the four sequences, suggesting that it was more effective than BM. Specifically, ABM_KF-K2 yielded error reductions of 1.93%, 15.60%, 16.41% and 63.03% for total displacements, compared to BM, for the sequences S_0, S_{25}, S_{15} and S_F, respectively.

The statistical significance of these results was validated following the process which is described below for each synthetic sequence. First, the root-mean-square (RMS) errors for total displacements for all the interrogated blocks were estimated, resulting in eight RMS error distributions (one for each method). Then, one-sample Kolmogorov–Smirnov tests indicated that the error distributions were not normal and, as a result, nonparametric tests were used for the statistical analysis. In a third step, a Kruskal–Wallis test showed that at least one error distribution was different from one of the others (p-values: 0.048, 0.047, 0.045 and 0.038 for the sequences S_0, S_{25}, S_{15} and S_F, respectively). Finally, a Wilcoxon rank-sum test between the error distributions of BM and ABM_KF-K2 indicated that the error reductions with respect to BM were statistically significant in most cases (p-values: 0.28, 0.042, 0.037 and 0.018 for the sequences S_0, S_{25}, S_{15} and S_F, respectively).

The selection of the most reliable algorithm was also affected by the performance of the presented motion estimators over different center frequencies. Table 3 presents bias and jitter [20], estimated as the mean and the standard deviation, respectively, of the warping indices for total displacements for different center frequencies. ABM_KF produced the lowest bias and ABM_KF-K2 the lowest jitter. ABM_KF-K2 produced the second lowest bias, suggesting the increased robustness of this algorithm. Compared to BM, ABM_KF-K2 yielded bias and jitter reductions of 30% and 64%, respectively.

In terms of the computational cost, tracking one block in an 87-image sequence required 10 s for BM, 51 s for ABM_KF and 53 s for ABM_KF-K2, using a Pentium(R) Dual-Core CPU T4400 at 2.20 GHz. However, the minimization of motion-tracking errors in most cases by ABM_KF-K2 and

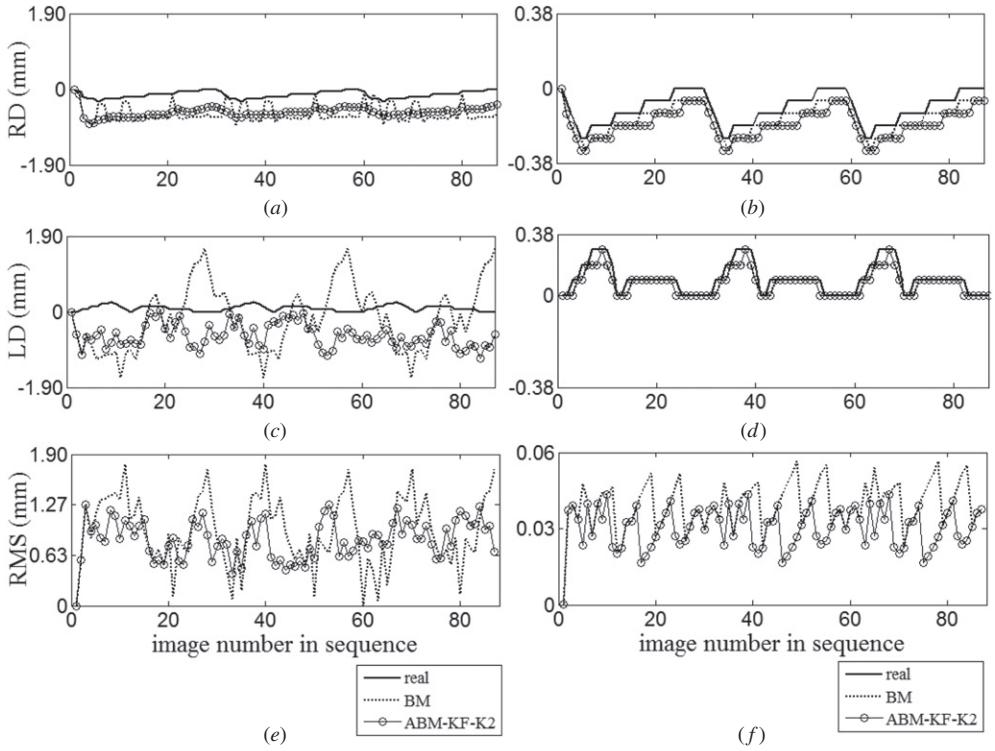

Figure 3. Radial (RD) (*a*), (*b*) and longitudinal (LD) (*c*), (*d*) displacements of a block located at the posterior wall–lumen interface in the first image of the synthetic sequences S_{15} (*a*), (*c*) and S_F (*b*), (*d*), using BM and ABM_KF-K2. RMS errors (*e*), (*f*) for total displacements. Different ranges were used for the *y*-axes for each sequence because of higher motion-tracking errors in the presence of noise.

Table 3. Bias and jitter (in mm) for BM, ABM_KF and combinations of them with K1 and K2, for varying center frequencies.

Algorithm	Bias	Jitter	Algorithm	Bias	Jitter
BM	0.235	0.147	ABM_KF	0.147	0.235
BM-K1	0.496	0.282	ABM_KF-K1	0.189	0.145
BM-K2	0.190	0.145	ABM_KF-K2	0.164	0.053
BM-K1-K2	0.496	0.282	ABM_KF-K1-K2	1.186	0.054

its robustness in varying image conditions compensated for the somewhat increased computational cost and the method was selected as the most reliable algorithm for the analysis of motion of the arterial wall from ultrasound images.

Figures 3(*a*)–(*d*) show examples of radial and longitudinal displacements of a block located at the posterior wall–lumen interface in the first image of the synthetic sequences S_{15} and S_F, using BM and ABM_KF-K2. The displacements in each direction were calculated by subtracting the positions of the block at end diastole. In both cases, ABM_KF-K2 produced radial and longitudinal displacements that were closer to real motion. In the longitudinal direction, in particular, ABM_KF-K2 resulted in smoother, less spiky waveforms, than BM. In figures 3(*a*) and (*b*), there is an almost constant difference between real motion and the waveform of ABM_KF-K2, which probably means that ABM_KF-K2 failed to find a similar block in the first images of the sequence and, as a result, the renewed reference blocks in subsequent images led the method to follow motion of a neighboring block. Figures 3(*e*) and (*f*) additionally illustrate the corresponding RMS errors for total displacements per image. The reduction in the mean value of RMS error of ABM_KF-K2, compared to BM, for these cases was 16.83% and 22.10%, respectively.

4.2. Real ultrasound image sequences

Considering that previous studies [1, 2] have shown that BM can detect the periodic motion pattern of the arterial wall from B-mode ultrasound, BM and ABM_KF-K2 were applied to real ultrasound image sequences to compare the produced radial and longitudinal displacements of selected blocks. Two blocks ('ANT' and 'POST') were selected on opposite wall–lumen interfaces (figure 2) and the displacement in each direction (figure 4) was calculated by subtracting the position of the block at end diastole, which in this case was identified from the minimum radial distance between ANT and POST. The waveforms produced using ABM_KF-K2 were generally similar to those produced using BM especially in terms of the expected periodic motion pattern. The BM waveforms seemed to produce somewhat more spikes than the KF ones. However, visual inspection of the sequences indicated rather regular motion patterns, closer to those produced by ABM_KF-K2.

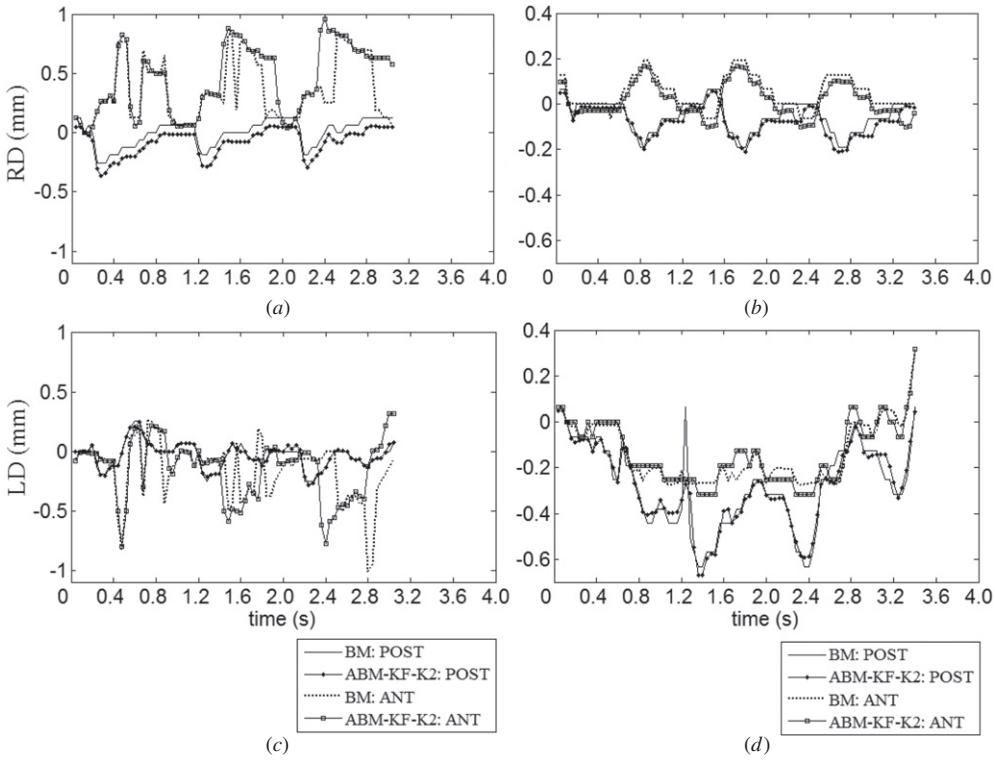

Figure 4. Examples of radial (*a*), (*b*) (RD) and longitudinal (LD) (*c*), (*d*) displacements of ANT and POST for a young (*a*), (*c*) and an elderly (*b*), (*d*) normal subject, using BM and ABM_KF-K2. Different ranges were used for the *y*-axes for each sequence to demonstrate the difference between BM and ABM_KF-K2.

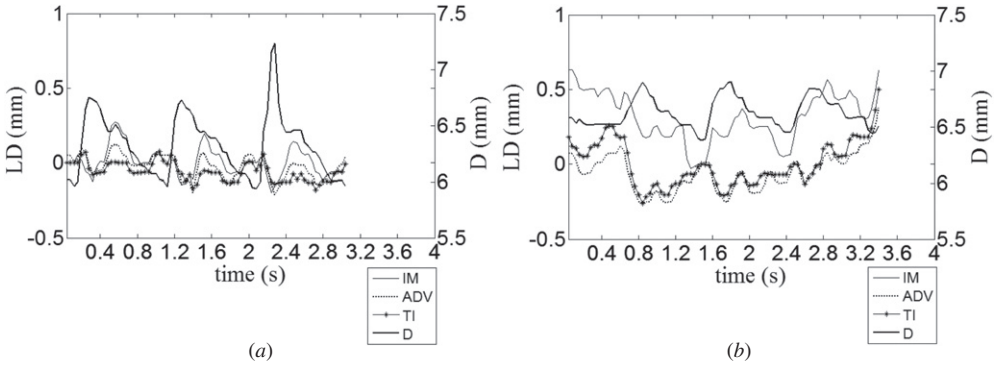

Figure 5. (*a*), (*b*) Longitudinal displacements (LD) (left axis) of the IM, ADV and TI and vessel diameter change (D) (right axis) for (*a*) a young and (*b*) an elderly normal subject, using ABM_KF-K2.

Table 4. Mean (±SD) values of strain parameters of the common carotid artery of five young and four elderly normal subjects during two or three consecutive cardiac cycles.

	Young ($n = 5$)	Elderly ($n = 4$)	All
Radial strain (%)	15.80 ± 3.06	7.56 ± 0.24	13.45 ± 4.73
Shear strain IM/ADV (rad)	0.34 ± 0.14	0.56 ± 0.04	0.41 ± 0.16
Shear strain ADV/TI (rad)	0.44 ± 0.23	0.16 ± 0.04	0.35 ± 0.23

Additionally, ABM_KF-K2 was used to obtain measurements of arterial strain in the radial and longitudinal directions (table 4), which were compared to those of similar studies. Specifically, the differences of radial motion waveforms of ANT and POST corresponded to vessel diameters (figure 5), which were used to estimate the radial strain [2], a measure of arterial elasticity. For the longitudinal direction, three blocks were selected at different layers of the posterior wall (figure 2): one block was positioned at the intima-media complex (IM), one block was positioned at the adventitial region (ADV), 0.45–0.76 mm deeper into the vessel wall than the block at IM, and one block was positioned at the surrounding tissue (TI), 0.51–0.83 mm deeper into the vessel wall than the block at ADV. The relative motion of

the selected blocks in the longitudinal direction (figure 5) introduced shear strain between the different layers, which was calculated using the formulas provided in [2]. Mean (±SD) values of these measurements for all recorded cycles of all subjects are presented in table 4.

Radial strain was significantly lower in elderly subjects compared to young ones (Wilcoxon rank-sum test, p-value: 0.014), implying an increase in radial arterial stiffness of the carotid artery with age, which is in agreement with existing knowledge [21]. Shear strain, on the other hand, was not significantly different between young and elderly subjects (Wilcoxon rank-sum test, p-value for both shear strains: 0.269). Strain measurements previously reported [2] were comparable to those of table 4. Specifically in [2], measurements in a group of ten healthy subjects (ages: 27–62 years) produced lower radial strains (10.6% ± 2.9). The shear strain between IM and ADV was 0.36 ± 0.26 rad, whereas the shear strain between ADV and TI was 0.49 ± 0.20 rad. No significant difference was found between the samples of the two studies in terms of the radial strain (p-value: 0.445) and the shear strain IM/ADV (p-value: 0.365). This finding demonstrates that the two sample sets probably originate from the same distribution and the differences in mean values may be attributed to differences in the age and/or the sex of the subjects.

5. Discussion

This work investigated the performance of KF-based approaches for BM in arterial wall motion estimation in an attempt to reduce motion-tracking errors of the BM algorithm, which is the conventional state of the art in the examined clinical application. It was found that the most effective method was ABM_KF-K2, which resulted from the incorporation of KF in BM as an update strategy for the reference block, combined with an update of the algorithm's motion estimate with K2. ABM_KF-K2 produced statistically significant reductions in motion-tracking errors in synthetic sequences, was tolerant to varying center frequencies and behaved well in real data experiments. Consequently, despite its somewhat higher computational cost compared with BM, it may be considered as an alternative to BM for motion analysis of the arterial wall from B-mode ultrasound.

The application of the investigated methods to synthetic data showed that in all cases the error increased when noise was added to the synthetic sequences. This may be due to the fact that noise reduces the image contrast and causes undesirable spatiotemporal changes in image intensities, thus preventing BM methods from finding the best-matched block. In most cases, errors were greater in the longitudinal direction probably because ultrasound imaging of the arterial wall shows higher homogeneity in that direction.

The warping indices showed that the combinations of BM with K1 and K2 were less effective than those of ABM_KF with these methods. This could be associated with the fact that ABM_KF takes into consideration changes in brightness of the image, which cannot be avoided because of the effect of speckle as well as the movement of the arterial wall out of the B-mode section. The superiority of ABM_KF-K2 could be attributed to the advantages of ABM_KF and the fact that K2 limits the displacement estimate according to the defined models. Such an update procedure probably prevents the transmission of considerable errors in the subsequent images.

Apart from minimizing motion-tracking errors in synthetic data experiments (table 2), ABM_KF-K2 also produced low bias and jitter when it was applied to synthetic image sequences with varying center frequencies. Bias and jitter have been widely used in the assessment of 1D motion estimators [20, 22]. Specifically, they have been used in the evaluation of different estimators of time delay between reference and reflected RF signals, assuming that these measurements result from changes in the displacements of acoustic scatterers. In this study, measurements of bias and jitter revealed that variable imaging conditions may affect the performance of motion estimators, considering that, although ABM_KF and ABM_KF-K2 produced comparable motion-tracking errors in the first set of synthetic sequences (table 2), the latter was considerably more robust in the second set of simulated data experiments (table 3). Investigation of the performance of the examined methods over other important imaging settings (such as electronic noise, bandwidth, persistence and dynamic range) and different image-to-image motion models would be an interesting future stage in this line of work.

Additionally, the precision of the above-mentioned 1D motion estimators was enhanced by incorporating interpolation techniques [23, 24], taking into account that time delays are generally not integral multiples of the sampling period. In the context of future work, further experimentations with modifications of the suggested methodology, including the application of interpolation techniques, might further enhance the validity of our method.

KF seems to be a useful computational tool in motion analysis of the arterial wall. The assumption of linearity for KF in (1) and (2) was considered reasonable in this initial attempt to address the specific problem, taking into account that (a) for ABM_KF, such an assumption produced satisfactory results in previous studies [5, 6] and (b) for K1/K2, there is no evidence in the literature for a validated image-to-image motion model for the carotid artery wall. However, an interesting future perspective of our study would be to replace the process model of K1 and K2, defined in (13), with the mathematical model which was used in the construction of the synthetic sequences [15] and investigate the effect of a nonlinear motion model on the performance of the examined methods in real data. In that case, KF would be replaced by extended or unscented KF, which are suitable to nonlinear and highly nonlinear systems, respectively [25].

In the context of real data experiments, ABM_KF-K2 produced the expected periodic motion waveforms when applied to real ultrasound image sequences of the carotid artery, a finding which enhanced its reliability. The measurements of radial and shear strain further reinforced this argument, because the results agreed with those of previous studies [2] and knowledge previously addressed in the literature [21]. Further experiments in additional samples

of normal subjects and patients would supplement both the investigation of the performance of ABM_KF-K2 in real image data and the provided knowledge about arterial wall motion.

Taking into consideration the synthetic and real data experiments, KF was effectively incorporated in BM, resulting in a sophisticated algorithm suitable for arterial tissue motion estimation. This method would be very useful in motion analysis of normal and diseased arterial segments during the cardiac cycle.

Acknowledgment

The work of AG was supported in part by the Hellenic State Scholarships Foundation.

References

[1] Golemati S, Sassano A, Lever M J, Bharath A A, Dhanjil S and Nicolaides A N 2003 Carotid artery wall motion estimated from B-mode ultrasound using region tracking and block-matching *Ultrasound Med. Biol.* **29** 387–99

[2] Cinthio M, Ahlgren A R, Bergkvist J, Jansson J T, Persson H W and Lindstrom K 2006 Longitudinal movements and resulting shear strain of the arterial wall *Am. J. Physiol. Heart Circ. Physiol.* **291** 394–402

[3] Bang J, Dahl T, Bruisna A, Kaspersen J H, Hernes T A N and Myhre H O 2003 A new method for analysis of motion of carotid plaques from RF ultrasound images *Ultrasound Med. Biol.* **29** 967–76

[4] Golemati S, Stoitsis J S, Perakis D A, Varela E, Alexandridi A, Davos C H and Nikita K S 2009 Carotid artery motion estimation from sequences of B-mode ultrasound images—effect of scanner settings and image normalization *IEEE Trans. Instrum. Meas.* **58** 2102–12

[5] Peacock A M, Matsunaga S, Renshaw D, Hannah J and Murray A 2000 Reference block updating when tracking with the block matching algorithm *IEEE Electron. Lett.* **36** 309–10

[6] Karayiannis B N, Sami A, Frost D J, Wise S M and Mizrahi M E 2005 Automated extraction of temporal motor activity signals from video recordings of neonatal seizures based on adaptive block matching *IEEE Trans. Biomed. Eng.* **52** 676–86

[7] Kuo C H, Chung S H and Shih P Y 2006 Kalman filtering based rate-constrained motion estimation for very low bit rate video coding *IEEE Trans. Circuits Syst. Video Technol.* **16** 3–18

[8] Michailovich O and Tannenbaum A 2006 A method for prediction and estimation of large-amplitude optical flows via extended Kalman filtering approach *Eng. Comput.* **23** 503–14

[9] Singh A 1992 Incremental estimation of image flow using the Kalman filter *J. Vis. Commun. Image Represent.* **3** 39–57

[10] Jacob G, Noble J A, Behrenbruch C, Kelion A D and Banning A P 2002 A shape-space-based approach to tracking myocardial borders and quantifying regional left-ventricular function applied in echocardiography *IEEE Trans. Med. Imaging* **21** 226–38

[11] Comaniciu D, Zhou X S and Krishnan S 2004 Robust real-time myocardial border tracking for echocardiography: an information fusion approach *IEEE Trans. Med. Imaging* **23** 849–60

[12] Orderud F 2006 A framework for real-time left ventricular tracking in 3D+T echocardiography, using nonlinear deformable contours and Kalman filter based tracking *Proc. IEEE Computers in Cardiology (Valencia, Spain)* pp 125–8

[13] Gastounioti A, Golemati S, Stoitsis J and Nikita K S 2010 Kalman-filter-based block matching for arterial wall motion estimation from B-mode ultrasound *Proc. IEEE Int. Conf. on Imaging Systems and Techniques (Thessaloniki, Greece)* pp 234–9

[14] Bozic S M 1980 *Digital and Kalman Filtering* (New York: Wiley)

[15] Stoitsis J, Golemati S, Koropouli V and Nikita K S 2008 Simulating dynamic B-mode ultrasound image data of the common carotid artery *Proc. IEEE Int. Workshop on Imaging Systems and Techniques (Chania, Greece)* pp 144–8

[16] Jensen J A 1996 Field: A program for simulating ultrasound systems *Med. Biol. Eng. Comput.* **34** 351–3

[17] Viola F and Walker W F 2005 A spline-based algorithm for continuous time-delay estimation using sampled data *IEEE Trans. Ultrason. Ferroelectr. Freq. Control* **52** 80–93

[18] Huang T and Tsai R 1981 *Image Sequence Analysis* (Berlin: Springer)

[19] Haworth C, Peacock A M and Renshaw D 2001 Performance of reference block updating techniques when tracking with the block matching algorithm *Proc. Int. Conf. on Image Processing (Thessaloniki, Greece)* pp 365–8

[20] Pinton G F and Trahey G 2006 Continuous delay estimation with polynomial splines *IEEE Trans. Ultrason. Ferroelectr. Freq. Control* **53** 2026–35

[21] Kawasaki T, Sasayama S, Yagi S I, Asakawa T and Hirai T 1987 Non-invasive assessment of the age related changes in stiffness of major branches of the human arteries *Cardiovasc. Res.* **21** 678–87

[22] Mauldin F W, Viola F and Walker W F 2010 Complex principal components for robust motion estimation *IEEE Trans. Ultrason. Ferroelectr. Freq. Control* **57** 2437–49

[23] de Jong P G M, Arts T, Hoeks A P G and Reneman R S 1990 Determination of tissue motion velocity by correlation interpolation of pulsed ultrasonic echo signals *Ultrason. Imag.* **12** 84–98

[24] Cespedes I, Huang Y, Ophir J and Spratt S 1995 Method for estimation of subsample time delays of digitized echo signals *Ultrason. Imag.* **17** 142–71

[25] Welch G and Bishop G 1995 An introduction to the Kalman filter *Technical Report TR95-041* University of North Carolina at Chapel Hill, NC, USA